

# A filtering approach based on Gaussian–powerlaw convolutions for local PET verification of proton radiotherapy

**Katia Parodi and Thomas Bortfeld**

Department of Radiation Oncology, Massachusetts General Hospital and Harvard Medical School, 30 Fruit Street, Boston, MA 02114, USA

E-mail: [kparodi@partners.org](mailto:kparodi@partners.org) and [tbortfeld@partners.org](mailto:tbortfeld@partners.org)

Received 19 August 2005, in final form 18 January 2006

Published 30 March 2006

Online at [stacks.iop.org/PMB/51/1991](http://stacks.iop.org/PMB/51/1991)

## Abstract

Because proton beams activate positron emitters in patients, positron emission tomography (PET) has the potential to play a unique role in the *in vivo* verification of proton radiotherapy. Unfortunately, the PET image is not directly proportional to the delivered radiation dose distribution. Current treatment verification strategies using PET therefore compare the actual PET image with full-blown Monte Carlo simulations of the PET signal. In this paper, we describe a simpler and more direct way to reconstruct the expected PET signal from the local radiation dose distribution near the distal fall-off region, which is calculated by the treatment planning programme. Under reasonable assumptions, the PET image can be described as a convolution of the dose distribution with a filter function. We develop a formalism to derive the filter function analytically. The main concept is the introduction of ‘ $\tilde{Q}$ ’ functions defined as the convolution of a Gaussian with a powerlaw function. Special  $\tilde{Q}$  functions are the Gaussian itself and the error function. The convolution of two  $\tilde{Q}$  functions is another  $\tilde{Q}$  function. By fitting elementary dose distributions and their corresponding PET signals with  $\tilde{Q}$  functions, we derive the  $\tilde{Q}$  function approximation of the filter. The new filtering method has been validated through comparisons with Monte Carlo calculations and, in one case, with measured data. While the basic concept is developed under idealized conditions assuming that the absorbing medium is homogeneous near the distal fall-off region, a generalization to inhomogeneous situations is also described. As a result, the method can determine the distal fall-off region of the PET signal, and consequently the range of the proton beam, with millimetre accuracy. Quantification of the produced activity is possible. In conclusion, the PET activity resulting from a proton beam treatment can be determined by locally filtering the dose distribution as obtained from the treatment planning system. The filter function can be calculated analytically using convolutions of Gaussians and powerlaw functions.

## 1. Introduction

Since therapeutic proton beams undergo nuclear interactions in tissue, and (p, xn) reactions such as the dominant (p, pn) channel may yield positron emitters such as  $^{11}\text{C}$  (half-life  $T_{1/2} = 20.39$  min) and  $^{15}\text{O}$  ( $T_{1/2} = 2.03$  min), positron emission tomography (PET) can be used as a unique tool to ‘image’ the treatment field *in vivo* (Bennett *et al* 1978, Vynckier *et al* 1993, Paans and Schippers 1993, Oelfke *et al* 1996, Litzenberg *et al* 1999, Parodi *et al* 2002, 2005, Hishikawa *et al* 2002, Nishio *et al* 2005). However, the PET image is not directly proportional to the delivered proton dose because of the different nuclear and atomic processes underlying  $\beta^+$ -activation and the dominant mechanism of energy deposition, respectively. An indirect way to verify particle beam dose delivery, which is pursued at the Gesellschaft für Schwerionenforschung Darmstadt, Germany, for carbon ion therapy (Enghardt *et al* 1999, 2004a), is to simulate the PET isotope activation and image formation on a computer (Pönisch *et al* 2004) and compare it with the actual PET image. If the two agree, one may have more confidence in the treatment. If they disagree, it is an indication that something went wrong in the delivery process, and further checks are required to understand and quantify the deviation (Enghardt *et al* 2004b).

To utilize the potential of proton therapy to its full extent, it is imperative that the distal dose fall-off is at its correct intended position. To verify this reliably, the PET calculation must currently include the initial beam phase space as well as all interactions between the skin entry and the maximum depth of penetration. Furthermore, the Monte Carlo simulation must model the electromagnetic and nuclear processes of relevance for dose calculation in full analogy to the treatment planning code, in order to provide a clinically meaningful comparison. Now, the distal fall-off of the PET signal is in close spatial proximity (within about 2–13 mm water equivalent, cf Nishio *et al* (2005)) to the distal fall-off of the dose distribution. Hence, if one could reconstruct the dose distribution directly and locally (i.e. in the last few centimetres of the delivered field) from the measured PET image, one would be insensitive to any error in the simulation of the entire beam penetration, e.g., due to artefacts of patient computed tomograms (CTs). The latter typically occur in the proximal part of the field outside the target volume and were found not to influence the accuracy of the PET measurement in the distal region of interest even when using CT-based attenuation corrections (this is currently under investigation in a separate study). Similarly, if one could reconstruct the expected PET image from the local calculated dose distribution near the distal fall-off, and it agrees with the measured PET image, one would have a more direct evidence that dose has been delivered at the right location. In the case of disagreement, this method provides a more direct evidence of a discrepancy between the treatment plan and the actual treatment delivery. The advantage is to rule out the uncertainties of the indirect comparison to the Monte Carlo PET simulation, which is not guaranteed to perfectly reproduce the treatment planning engine, especially when the latter is based on analytical pencil-beam models. This issue is particularly critical for proton beams because of their considerable lateral scattering.

In the following, we will describe a mathematical formalism with the help of which we may attempt such a *local* reconstruction. The formulation of the PET verification issue as a convolution (filtering) problem under idealized conditions of medium homogeneity is presented in section 2. The mathematical modelling is addressed in section 2.1. Section 2.2 introduces the Gaussian and powerlaw convolution framework. The analytical calculation of a specific filter allowing the local PET reconstruction on the basis of the introduced framework is presented in section 2.3. The application of the described formalism to real PET data measured in a homogeneous phantom experiment is reported in section 3. The generalization of the method to inhomogeneous media and other reaction channels is addressed in section 4.

A discussion of the proposed approach and obtained results is presented in section 5. Section 6 concludes the paper.

## 2. The PET verification problem under idealized conditions

### 2.1. Mathematical formulation of the filtering approach

To make things simple, we will first consider a quasi one-dimensional case, i.e., a case without lateral variation of the beam or the phantom. Also, for now we will restrict ourselves to the consideration of targets that are homogeneous in the relevant distal fall-off region. A generalization to heterogeneous situations will be described in section 4.

Let  $P(z)$  be the irradiation-induced PET activity along the depth  $z$ . By definition, we can write this as the superposition of PET activation  $p(z, E)$  differential in initial proton energy  $E$ , i.e.,  $p(z, E)$  is the PET activation for a mono-energetic beam:

$$P(z) = \int_0^{\infty} w_E(E) p(z, E) dE, \quad (1)$$

where  $w_E(E)$  is the energy spectrum of the beam. We can then replace the energy by the nominal range  $R$ :

$$P(z) = \int_0^{\infty} w(R) p(z, R) dR, \quad (2)$$

where  $w(R) = w_E(E(R)) dE/dR$ .

In a similar way, we can describe the total dose distribution  $D(z)$  as a superposition of individual Bragg peak distributions  $b(z, R)$ :

$$D(z) = \int_0^{\infty} w(R) b(z, R) dR. \quad (3)$$

Under the assumptions made above, both  $p(z, R)$  and  $b(z, R)$  are shift invariant, at least locally near the distal fall-off region of  $P(z)$  and  $D(z)$ . That means  $p(z, R) = p(z - R)$  and  $b(z, R) = b(z - R)$ . The validity of this approximation was verified through FLUKA Monte Carlo calculations (Fassò *et al* 2001a, 2001b), using experimental cross sections for positron emitter production (Parodi *et al* 2002). This approach, which had previously been validated against experimental data (Parodi *et al* 2002, 2005), was extended to include reactions such as  $^{16}\text{O}(p, 3p3n)^{11}\text{C}$  (Albouy *et al* 1962) in addition to the main (p, pn) channels on carbon and oxygen nuclei. The simulated positron emitter distributions  $p_i(z, R)$  were smoothed with a three-dimensional Gaussian point spread function (psf) of 7 mm FWHM, accounting for the typical 5–7 mm FWHM spatial resolution of commercial whole-body PET scanners. Examples are shown in figures 1 and 2 for irradiation with mono-energetic, pencil-like (6 mm FWHM) beams of  $10^4$  primary protons. Activity and depth dose profiles,  $b_i(z, R)$ , are integrated over the entire lateral extension of the field. Figure 1 demonstrates the validity of the local shift invariance assumption and its independence from the initial beam energy within the clinically relevant 70–230 MeV interval. Figure 2 shows the independence from the absorber material, involving different reaction channels for  $\beta^+$ -activity production. The depicted shifted curves are almost indistinguishable in the distal part, except for a slight decrease in the height of both dose and activity profiles for increasing beam energy, which is due to range straggling and nuclear reaction effects.

Within the assumption of shift invariance, equations (2) and (3) become convolution integrals:

$$P(z) = \int_0^{\infty} w(R) p(z - R) dR = w(z) * p(z), \quad (4)$$

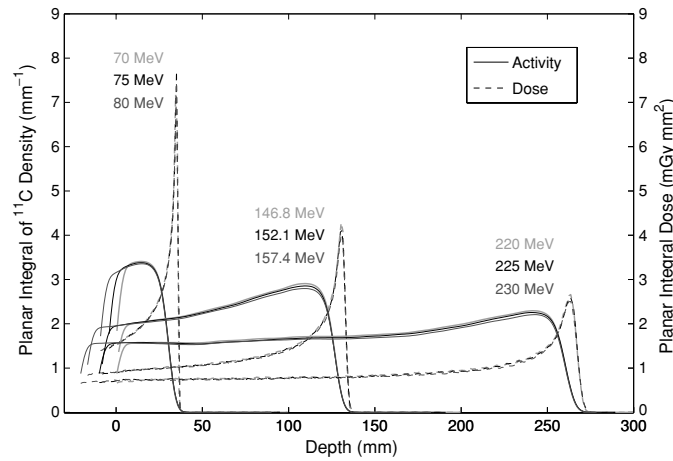


**Figure 1.** Depth energy deposition (dashed) and corresponding <sup>11</sup>C activation (solid) calculated in polymethyl methacrylate (PMMA) for three groups of three close initial energies distributed in the entire interval of therapeutic relevance. Within each group, the dose and activity profiles at intermediate (black) and high (dark grey) energies were shifted backwards in space to adjust the Bragg peak position to that of the lowest energy (light grey) contribution.

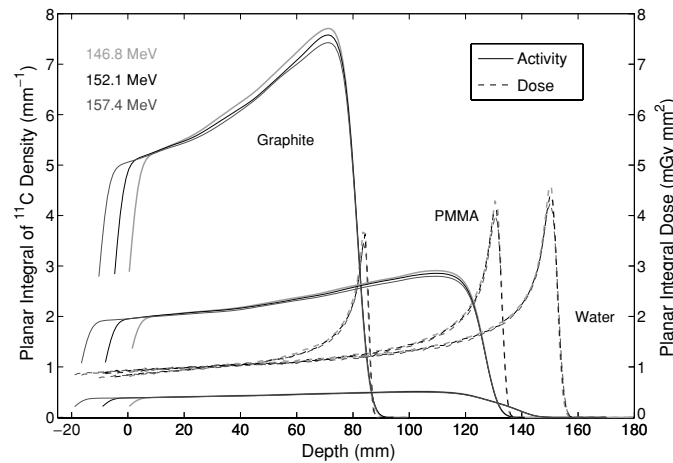


**Figure 2.** Depth energy deposition (dashed) and corresponding <sup>11</sup>C activation (solid) in graphite, PMMA and water for three similar initial proton beam energies. As in figure 1, the middle (black) and high (dark grey) energy profiles were adjusted to the penetration depth of the lowest energy (light grey) contribution.

$$D(z) = \int_0^{\infty} w(R)b(z-R) dR = w(z) * b(z), \quad (5)$$

where \* stands for a one-dimensional convolution. Then, we can easily show that

$$P(z) = D(z) * f(z) = \int_{-\infty}^{\infty} D(z')f(z-z') dz', \quad (6)$$

where  $f(z)$  is defined indirectly by

$$b(z) * f(z) = p(z). \quad (7)$$

To show this, just combine equations (4) and (5) to  $P = D * b^{-1} * p$  and insert equation (7). It should be noted that shift invariance of  $p$  and  $b$  is not a necessary condition for equation (7). In fact, in real cases we will see that equation (7) holds even though the shift invariance of  $p$  and  $b$  is not exactly fulfilled. The physical reason will be addressed in section 4.

The bottom line is that the PET image can be obtained by convolving (filtering) the dose distribution with a filter  $f$ . Of course, with an inverse filter  $f^{-1}$  we could calculate  $D(z) = P(z) * f^{-1}(z)$ .

We will now show that equation (6) is indeed a local operation. First, let  $z_{\max}$  be the depth beyond which  $P(z)$  is practically zero. Let  $z_{\max} + \epsilon$  be the depth beyond which  $D(z)$  is practically zero (as already said,  $\epsilon$  is in the order of 2–13 mm in water). Then it is clear that the upper limit of the integral in equation (6) is  $z_{\max} + \epsilon$ . Also, that  $P(z)$  is zero for  $z > z_{\max}$  but  $D(z')$  is  $\neq 0$  for  $z' < z_{\max} + \epsilon$  implies that  $f(z - z')$  is zero for  $z - z' > -\epsilon$ . Hence, the lower limit of the integral in equation (6) is  $z' = z + \epsilon$ , and we obtain

$$P(z) = \int_{z+\epsilon}^{z_{\max}+\epsilon} D(z')f(z - z') dz'. \tag{8}$$

Consequently, we find that a local operator can indeed estimate the PET signal. If we want to know  $P(z)$  in the distal range, say between  $z_{\max} - \Delta$  and  $z_{\max}$ , we need to determine  $f(z)$  in the interval  $[-\Delta - \epsilon, -\epsilon]$  only. Mathematical tools that allow us to derive the filter in equation (7) will be developed next.

2.2. The Gaussian and powerlaw convolution framework

The determination of the filter in equation (7) is a deconvolution problem. The following formalism will allow us to solve this problem analytically. First, we define a set of functions  $\tilde{Q}_\nu(x)$  as the convolution of a Gaussian

$$G(x) = \frac{1}{\sqrt{2\pi}} \exp\left(-\frac{x^2}{2}\right) \tag{9}$$

and a powerlaw

$$P_\nu(x) = \begin{cases} \frac{1}{\Gamma(\nu)}x^{\nu-1}, & \text{if } x \geq 0, \\ 0, & \text{otherwise,} \end{cases} \tag{10}$$

in which the gamma function,  $\Gamma(\nu)$ , is used for normalization purposes. Recall that the gamma function is an extension of the factorial (!) to real number arguments. If the argument,  $\nu$ , is an integer, then  $\Gamma(\nu) = (\nu - 1)!$ . Note that  $\Gamma(\nu)$  has a singularity at  $\nu = 0$ . For  $\nu = 0$ , the function  $P_\nu(x)$  becomes a Dirac delta function. This is easy to show using the definition of the gamma function.

There exists a closed form solution of the convolution integral in terms of parabolic cylinder functions,  $\mathcal{D}$  (cf appendix in Bortfeld (1997) and Gradshteyn and Ryzhik (1980)):

$$\tilde{Q}_\nu(x) = G(x) * P_\nu(x) \tag{11}$$

$$= \frac{1}{\sqrt{2\pi}} \frac{1}{\Gamma(\nu)} \int_0^\infty \exp\left(-\frac{(x-x')^2}{2}\right) x'^{\nu-1} dx' \tag{12}$$

$$= \frac{1}{\sqrt{2\pi}} \exp\left(-\frac{x^2}{4}\right) \mathcal{D}_{-\nu}(-x). \tag{13}$$

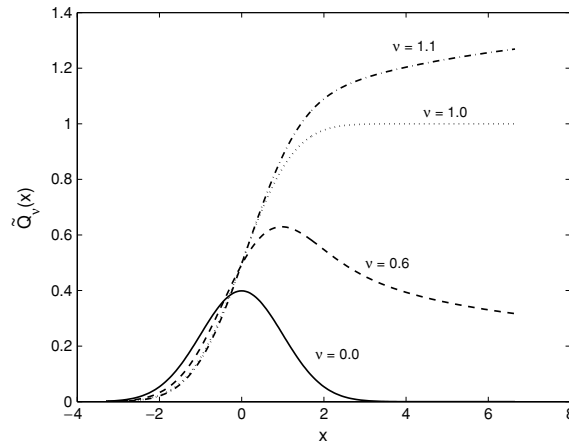


**Figure 3.** Plots of functions  $\tilde{Q}_\nu(x)$  for  $\nu = 0.0, 0.6, 1.0$  and  $1.1$ . With  $\nu = 0$  we obtain a Gaussian, and with  $\nu = 1$  an error function.

The function  $\tilde{Q}_\nu(x)$  has a number of interesting characteristics. First, depending on the parameter  $\nu$ , the set of  $\tilde{Q}_\nu(x)$  includes the Gaussian and the error function. Based on equation (13),  $\tilde{Q}_\nu(x)$  is well defined for  $\nu = 0$ , in which case we obtain the Gaussian

$$\tilde{Q}_0(x) = \frac{1}{\sqrt{2\pi}} \exp\left(-\frac{x^2}{2}\right) = G(x). \quad (14)$$

With  $\nu = 1$  we get the probability integral, which can be expressed through the error function,  $\text{erf}(x)$ :

$$\tilde{Q}_1(x) = \frac{1}{2} + \frac{1}{2} \text{erf}\left(\frac{x}{\sqrt{2}}\right). \quad (15)$$

Setting  $\nu \approx 0.6$  yields the depth dose distribution of a therapeutic proton beam (Bortfeld 1997). The graphs of  $\tilde{Q}_\nu(x)$  for these different values of  $\nu$  are shown in figure 3.

Another useful feature of  $\tilde{Q}_\nu(x)$  is that the convolution of two  $\tilde{Q}_\nu$  functions is a  $\tilde{Q}_\nu$  function again. Specifically,

$$\tilde{Q}_{\nu_1}(x) * \tilde{Q}_{\nu_2}(x) = \sqrt{2}^{\nu_1+\nu_2-1} \tilde{Q}_{\nu_1+\nu_2}\left(\frac{x}{\sqrt{2}}\right). \quad (16)$$

The reason is that the convolution of two  $P$  functions yields another  $P$  function, and, of course, the convolution of two Gaussians yields another Gaussian.

If we consider scaled and shifted versions of  $\tilde{Q}_\nu$  functions, we obtain the more general result:

$$\tilde{Q}_{\nu_1}\left(\frac{x-a_1}{\sigma_1}\right) * \tilde{Q}_{\nu_2}\left(\frac{x-a_2}{\sigma_2}\right) = \frac{\sqrt{\sigma_1^2 + \sigma_2^2}^{\nu_1+\nu_2-1}}{\sigma_1^{\nu_1-1} \sigma_2^{\nu_2-1}} \tilde{Q}_{\nu_1+\nu_2}\left(\frac{x-a_1-a_2}{\sqrt{\sigma_1^2 + \sigma_2^2}}\right). \quad (17)$$

Proofs are given in the appendix.

### 2.3. The calculation of the filter function

The explicit calculation of the filter function using the Gaussian–powerlaw convolution formalism is presented here for the specific activation study of a homogeneous target of

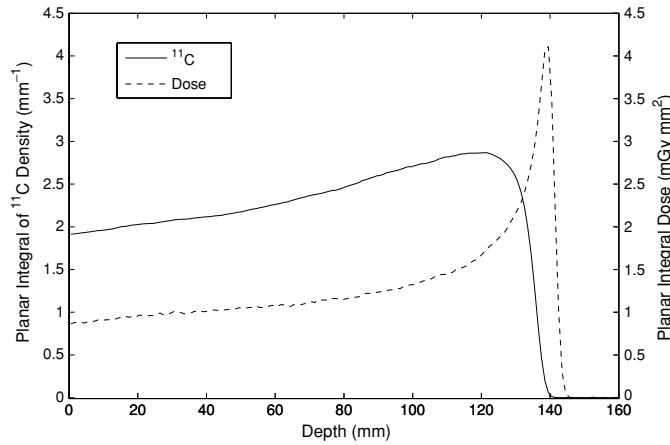


**Figure 4.** Monte Carlo calculation of the laterally integrated energy deposition (dashed) and corresponding  $^{11}\text{C}$  depth distribution (solid) for  $10^4$  protons stopped in PMMA at 152.1 MeV initial energy.

polymethyl methacrylate (PMMA, composition:  $\text{C}_5\text{H}_8\text{O}_2$ , density:  $1.18 \text{ g cm}^{-3}$ ). Since we are interested in the practical application to off-line PET imaging, we will only look at the longer lived  $^{11}\text{C}$  component. Section 4 will then show that the generalization of the proposed filtering method to arbitrary materials requires only a small number of reaction-dependent filter functions that need to be calculated in reference media such as PMMA for the isotopes of interest.

Due the assumption of shift invariance, we can take any pair of  $p(z, R)$ ,  $b(z, R)$  functions for a specific  $R$  to determine  $f(z)$  according to equation (7).

$$p(z, R) = b(z, R) * f(z) = \int_{z+\epsilon}^{z_{\max}+\epsilon} b(z', R) f(z - z') dz'. \quad (18)$$

$p(z, R)$  needs to be known in the  $z$ -interval  $[z_{\max} - \Delta, z_{\max}]$  and  $b(z, R)$  in the interval  $[z_{\max} + \epsilon - \Delta, z_{\max} + \epsilon]$ .

We use the  $p(z, R)$  and  $b(z, R)$  distributions calculated with the Monte Carlo technique described in section 2.1 at the intermediate energy of 152.1 MeV. The positron emitter and energy deposition depth profiles depicted in figure 4 were integrated over the whole lateral field extension mainly to improve counting statistics. In addition, for very small fields such as the 6 mm (FWHM) pencil beam of figure 4, the different amount of particle loss due to scattering along the different distal penetration depth of the dose and of the PET signal may affect the amplitude of the filter function in dependence on the integration region. In this specific example, deviations up to 17% occur when the integration region is made as small as  $1 \text{ mm}^2$ . The problem does not exist in real broad beams, as will be shown. In contrast to figure 1, no smoothing was applied to the simulated isotope distribution. Instead, the point spread function accounting for the response of the imaging system will be applied after the filtering of the dose distribution with  $f(z)$ . This detail will become important when we consider inhomogeneous materials in section 4.

We performed a least-squares fit of the  $\tilde{Q}$  functions to the Monte Carlo data. The fit parameters were the shape parameter ( $\nu$ ), the scale parameter ( $\sigma$ ), the shift ( $a$ ) (see

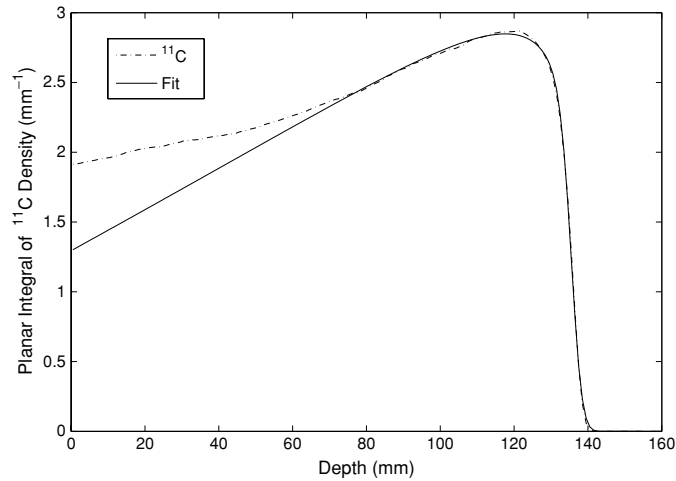


**Figure 5.** Fit (solid) of the  $^{11}\text{C}$  signal (dash-dotted) with two  $\tilde{Q}$  functions in the depth range between  $z = 71$  mm and  $z = 141$  mm. See equation (19).

equation (17)) and an overall normalization factor. The fit was done using the Matlab<sup>1</sup> ‘fminsearch’ routine.

It turned out that the PET data could not be reasonably fitted with a single  $\tilde{Q}$  function. However, with two  $\tilde{Q}$  functions with the same  $a$  and  $\sigma$  but different  $\nu$ , a good fit could be achieved in the relevant depth range between  $z = 71$  mm and  $z = 141$  mm, i.e., for  $\Delta = 70$  mm:

$$p(z, R) \approx 4.6313 \text{ mm}^{-1} \tilde{Q}_{1.3353} \left( \frac{-z + 136 \text{ mm}}{2.18 \text{ mm}} \right) - 2.5769 \text{ mm}^{-1} \tilde{Q}_{1.4596} \left( \frac{-z + 136 \text{ mm}}{2.18 \text{ mm}} \right). \quad (19)$$

This fit is shown in figure 5. With three  $\tilde{Q}$  functions, a nearly perfect fit is achievable everywhere down to  $z = 0$ . However, this is not necessary as we are only interested in the distal parts of the PET signal and the dose.

The depth dose was fitted in the depth range between  $z = 76$  mm and  $z = 146$  mm with the  $\tilde{Q}$  function

$$b(z, R) \approx 6.46 \text{ mGy mm}^2 \tilde{Q}_{0.625} \left( \frac{-z + 140.7 \text{ mm}}{1.53 \text{ mm}} \right). \quad (20)$$

Here we show the fit in figure 6.

With equation (7) and with the help of the general convolution relationship for  $\tilde{Q}$  functions from equation (17), it is now a simple exercise to calculate the filter  $f(z)$ :

$$f(z) \approx 0.4143 \text{ mGy}^{-1} \text{ mm}^{-4} \tilde{Q}_{0.7103} \left( \frac{-z - 4.7 \text{ mm}}{1.553 \text{ mm}} \right) - 0.2210 \text{ mGy}^{-1} \text{ mm}^{-4} \tilde{Q}_{0.8346} \left( \frac{-z - 4.7 \text{ mm}}{1.553 \text{ mm}} \right), \quad (21)$$

as displayed in figure 7. This analytical deconvolution will only work if  $\sigma$  used in the fit of  $p(z, R)$  is bigger than  $\sigma$  used in  $b(z, R)$ . The same restriction applies to  $\nu$ .

<sup>1</sup> The MathWorks Inc., Natick, MA.

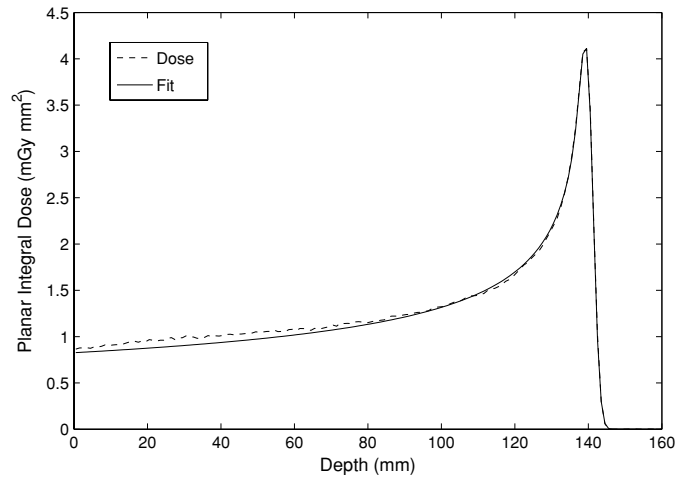


**Figure 6.** Fit (solid) of the laterally integrated dose distribution (dashed) with a  $\tilde{Q}$  function in the depth range between  $z = 76$  mm and  $z = 146$  mm. See equation (20).

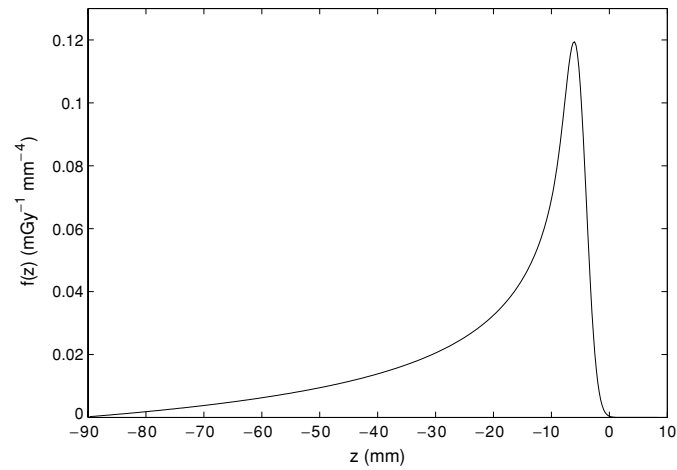


**Figure 7.** Graph of the filter function  $f(z)$ . See equation (21).

For validation, the filter  $f(z)$  was applied to the calculated dose distributions at three initial beam energies. The resulting  $^{11}\text{C}$  distributions are plotted against the Monte Carlo predictions in figure 8, which demonstrates the agreement in the distal fall-off region of the profiles in absolute terms. No normalization or scaling factor was applied. The discrepancy in the entrance channel reflects the limitation of the fit of figure 5. As already mentioned, the discrepancy can be avoided by using three  $\tilde{Q}$  functions.

The figure shows that the same filter can be applied over the whole range of therapeutically relevant depths. Interestingly, the shift invariance assumption is not valid over this extended range. In fact, it can strictly be shown that the filtering approach does also work with relaxed assumptions. In combination with the linearity of the convolution operator, the uniqueness of the filter guarantees the method to be directly applicable to extended dose distributions, i.e. formed by the superimposition of several mono-energetic beams, to obtain the corresponding integral activity distribution, as will be shown next.

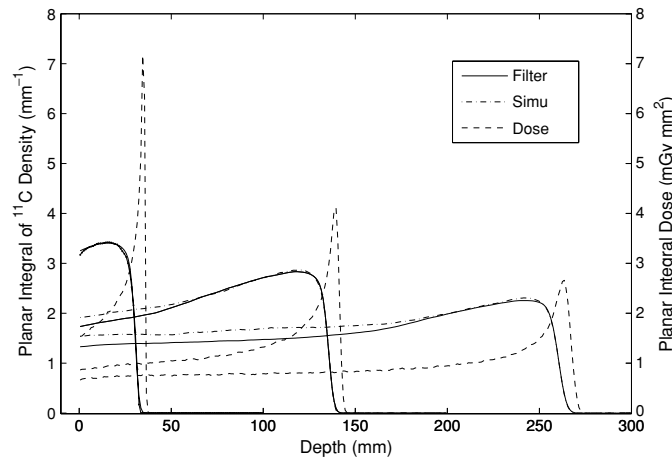


**Figure 8.**  $^{11}\text{C}$  depth distributions (solid) obtained from the application of the filter  $f(z)$  of figure 7 to the calculated depth dose profiles (dashed) in comparison with the positron emitter Monte Carlo predictions (dash-dotted) for three mono-energetic proton beams ( $10^4$  primaries) stopped in PMMA at 70, 152.1 and 220 MeV, respectively. No normalization factor was applied. The good agreement implies that the same filter can be applied to reconstruct the distal fall-off at a large range of depths.

### 3. The application to measured data for a homogeneous target

The proposed filtering approach was compared with real PET data measured in phantom activation studies after proton irradiation at the Proton Therapy Center at Massachusetts General Hospital, Boston. Details and results of these experiments will be reported in a separate paper. Here we irradiated a PMMA cylinder phantom (89 mm radius, 204 mm height) from the top with a dose of 8 Gy. The field was a spread-out Bragg peak (SOBP) of  $80 \times 80 \text{ mm}^2$  aperture, 160 mm water-equivalent range and 100 mm water-equivalent modulation. The induced activation was imaged for 1 h starting about 20 min after the irradiation end at a PET/CT scanner (CPS/Siemens Biograph Sensation 16) located in the hospital within a 10 min walking distance from the proton therapy unit. Absolute quantification was obtained from filtered back projection data, including all necessary correction factors for attenuation, random and scattered coincidences, detection efficiency and dead time as well as eliminating any decay correction applied by the scanner. To improve the accuracy of the estimation, several dynamic reconstructions of the acquired listmode data sampled in 1, 2, 5 and 20 min time frames, respectively, were compared and analysed. Decay time analysis of the measured listmode data as well as of the dynamically reconstructed distributions in regions of interest allowed us to separate the different isotope contributions to the activity, clearly dominated ( $\approx 95\%$  at the beginning of imaging) by  $^{11}\text{C}$  decays. For visualization, the final PET image was reconstructed from the whole data acquisition to improve counting statistics. The intensity was normalized to the absolute activity *at the beginning* of imaging, corrected for the  $^{11}\text{C}$  fraction resulting from the decay time analysis. Uncertainties were estimated to be within 4%.

In this specific case, the planned dose distribution was calculated with Monte Carlo using the FLUKA code. The phase space input information was obtained from a GEANT4 (Agostinelli *et al* 2003) based simulation, which models the entire nozzle of the facility (Paganetti *et al* 2004). The dose calculation approach was validated in water against depth dose measurements taken with an ionization chamber in a water tank. To provide good counting

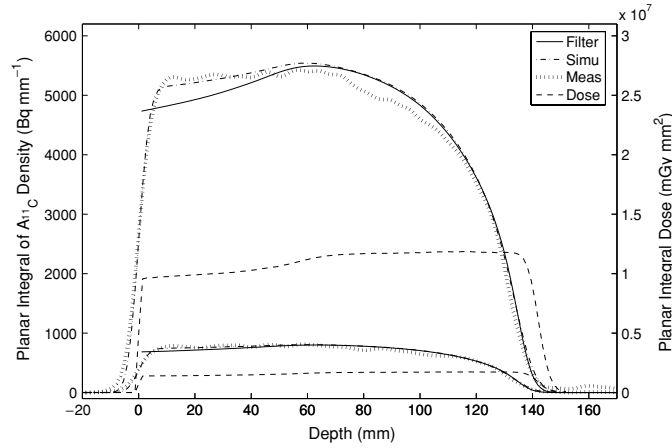


**Figure 9.** Measured  $^{11}\text{C}$  activity signals (thick dotted lines) in comparison with the predictions (solid) based on equation (7), the filter from figure 7, equation (22) and the planned dose profiles (dashed). The results of a complete Monte Carlo simulation are also shown (dash-dotted). All data were obtained from distributions integrated over two different lateral regions:  $\pm 7.5$  mm (lower curves) and  $\pm 19.5$  mm (upper curves) from the central axis.

statistics within a reasonable computational time, the FLUKA Monte Carlo simulation in PMMA was performed for about  $2.2 \times 10^6$  primary protons and normalized to the prescribed dose to water in the SOBP. The normalization factor was deduced from the calculations in water using the same number of primaries from the same phase space.

The predicted absolute amount of  $^{11}\text{C}$  isotopes produced per unit path length,  $N_{^{11}\text{C}}$ , was obtained by applying the filter  $f(z)$  calculated in section 2.3 (cf figure 7) to the Monte Carlo planned dose distribution. From  $N_{^{11}\text{C}}$  the expected depth activity contribution of  $^{11}\text{C}$  at the beginning of the acquisition,  $A_{^{11}\text{C}}$ , was determined as

$$A_{^{11}\text{C}} = N_{^{11}\text{C}} \frac{(1 - e^{-\lambda_{^{11}\text{C}} t_{\text{irr}}})}{t_{\text{irr}}} e^{-\lambda_{^{11}\text{C}} \Delta t}, \quad (22)$$

where  $\lambda_{^{11}\text{C}}$  is the  $^{11}\text{C}$  decay constant ( $\approx 5.67 \times 10^{-4} \text{ s}^{-1}$ ),  $t_{\text{irr}}$  is the time duration of the irradiation ( $\approx 360$  s) and  $\Delta t$  is the time interval between the end of irradiation and the beginning of imaging (cf Parodi *et al* (2002)). A Gaussian psf of 7 mm FWHM was finally applied to take into account blurring effects due to the image formation (positron and photon propagation) and reconstruction.

Measured, filtered and Monte Carlo calculated  $^{11}\text{C}$  activity distributions are compared in figure 9. All measured and calculated activity profiles are extracted from data integrated over two different lateral regions:  $\pm 7.5$  mm (lower curves) and  $\pm 19.5$  mm (upper curves) from the field central axis.

#### 4. The generalization to inhomogeneous media

An extension of the given formalism to more realistic situations must take into account the dependence of the induced activation on the tissue composition and density, as well as the specifics of the time course of irradiation and imaging. We will be mainly concerned with depth variations of the material composition. The lateral PET activity distribution correlates well with the energy deposition because of the direct proportionality of both quantities to the particle fluence. Millimetre agreement between lateral activity and lateral dose profiles was

also experimentally demonstrated (Oelfke *et al* 1996, Nishio *et al* 2005, Parodi *et al* 2005). In the following, we will focus on our most relevant time scenario, namely off-line imaging at a cyclotron-based proton facility with passive beam shaping systems.

#### 4.1. The generalized mathematical formulation of the filtering approach

In section 2.1, we derived the convolution (filtering) formulation of equation (7) from the assumption of local shift invariance of the PET and dose signal. For this particular mathematical derivation, we had to restrict our consideration to an absorbing medium which is homogeneous, at least locally near the distal fall-off region, to ensure the local validity of the shift invariance assumption. However, we saw in section 2.3 that the formalism holds even when the shift invariance condition is not necessarily fulfilled. Indeed, the two main physical quantities determining the PET and dose signal for a given proton fluence are the nuclear cross sections and the stopping power, respectively. Hence, a more general physical interpretation of the filtering formulation can be related to the dependence of cross sections and stopping power on the residual energy spectrum of the protons as they slow down. Since the same energy spectrum corresponds to different residual ranges in different materials, the applicability of a unique filter function to different media can be restored when stretching the spatial distributions to the equivalent path length in the material for which the filter function was defined. This can be achieved in analogy to the water-equivalent range-conversion formalism well established in particle treatment planning (Hong *et al* 1996), where the water-equivalent path length  $l_w$  is defined as

$$l_w(z) = \int_0^z \frac{\rho_{el}(z')}{\rho_{el,w}} dz', \quad (23)$$

in which  $\rho_{el}(z')/\rho_{el,w}$  is the electron density of the traversed medium at depth  $z'$  relative to water. In contrast to the treatment planning approach, we only need a local path length operator  $\mathcal{F}$  that will be applied to the distal region of interest  $[z_{\min}, z_{\max}]$ :

$$\mathcal{F} : z \rightarrow z^* = \int_{z_{\min}}^z \frac{\rho_{el}(z')}{\rho_{el,ref}} dz', \quad z_{\min} \leq z \leq z_{\max}, \quad (24)$$

where  $\rho_{el,ref}$  is the electron density of the reference material for which the filter function was calculated.

Therefore, the dose function  $D^*$  to be filtered in the depth-equivalent space  $z^*$  can be obtained as

$$D^*(z^*) = D^*(\mathcal{F}(z)) = D(z), \quad (25)$$

where  $D(z)$  is the original planned dose.

Since more reaction channels can be involved in realistic cases, corresponding filter functions  $f_i$  must be defined in reference media according to the calculation method presented in section 2.3. The weight of each reaction channel,  $i$ , in dependence on the original (i.e., at depth  $z$  in the real space) tissue composition and the time course of irradiation and imaging, can be finally introduced by a local factor  $g_i(z, t)$ :

$$g_i(z, t) = \left[ \frac{w_i(z)\rho(z)}{w_{i,ref}\rho_{ref}} \right] \left[ \frac{\rho(z)\rho_{el,ref}}{\rho_{el}(z)\rho_{ref}} \right] \left[ \frac{(1 - e^{-\lambda_i t_{irr}})}{t_{irr}} e^{-\lambda_i(\Delta t + t - t_0)} \right], \quad t \geq t_0. \quad (26)$$

Here  $w_i(z)/w_{i,ref}$  is the fraction by weight of the target nucleus involved in the given reaction channel in the considered material at depth  $z$  relative to the reference material for which the filter function was obtained,  $\rho(z)/\rho_{ref}$  and  $\rho_{el}(z)/\rho_{el,ref}$  are the mass and electron density of the material at depth  $z$  relative to the reference material, respectively,  $\lambda_i$  is the decay constant

of the produced positron emitter and  $t_0$  is the start time of the acquisition. The normalization factor in the first bracket accounts for the activation dependence on the nuclear density. The second factor introduces a correction for the energy deposition, which depends on the electron density rather than mass density. The third factor accounts for the time dynamics of the activity formation and decay, similarly to equation (22). In contrast to it, however, it calculates the activity at the considered time  $t$  rather than the activity at the beginning of the acquisition (see also Parodi *et al* (2002, 2005)).

Following all these considerations, equation (6) can be finally generalized to

$$P(z, t) = \sum_i g_i(z, t) p_i(z), \quad (27)$$

with

$$p_i(z) = p_i(\mathcal{F}^{-1}(z^*)) = p_i^*(z^*), \quad (28)$$

where  $\mathcal{F}^{-1}$  is the inverse transformation of equation (24) and  $p_i^*(z^*)$  results from the filtering of the dose in the depth-equivalent space:

$$p_i^*(z^*) = D^*(z^*) * f_i(z^*). \quad (29)$$

Now it is evident that the PET system point spread function has to be applied to  $P(z, t)$  in ‘real’ space after the  $\mathcal{F}^{-1}$  transformation of  $p_i^*(z^*)$ . Therefore, it should not be directly included in the filter function itself.

#### 4.2. The application to inhomogeneous targets

For validation of the proposed generalization, the individual filters corresponding to the  $^{12}\text{C}(\text{p}, \text{pn})^{11}\text{C}$  and  $^{16}\text{O}(\text{p}, 3\text{p}3\text{n})^{11}\text{C}$  reaction channels were calculated according to the method described in section 2.3. We used the simulated separate isotope depth distributions  $p_i(z, R)$  leading to the total  $^{11}\text{C}$  production in PMMA of figure 4 for the same depth dose profile  $b(z, R)$  at the intermediate energy of 152.1 MeV. The resulting filtered distributions are compared to the used Monte Carlo predictions  $p_i(z, R)$  in figure 10. Again the disagreement in the entrance channel is ascribed to the limitation of the fit to two  $\tilde{Q}_v$  functions and can be removed when extending the fit to three functions (cf section 2.3).

The two filter functions  $f_{\text{C,p,pn}}$  and  $f_{\text{O,p,3p3n}}$  obtained in PMMA were first applied to dose distributions calculated for mono-energetic proton irradiation of homogeneous graphite (C,  $\rho = 2.0 \text{ g cm}^{-3}$ ,  $\rho_{\text{el}}/\rho_{\text{el,PMMA}} = 1.5587$ ), polyethylene ( $\text{CH}_2$ ,  $\rho = 0.93 \text{ g cm}^{-3}$ ,  $\rho_{\text{el}}/\rho_{\text{el,PMMA}} = 0.8638$ ) and water ( $\text{H}_2\text{O}$ ,  $\rho = 1.0 \text{ g cm}^{-3}$ ,  $\rho_{\text{el}}/\rho_{\text{el,PMMA}} = 0.8746$ ) targets at several beam energies. This choice allows us to validate the stretching and weighting formalism of equation (27) for the two separate reaction channels. Since the same  $^{11}\text{C}$  isotope is concerned, we did not include the time correction for the activity formation and decay (third bracket of equation (26)) in the weighting factors  $g_i$ . Basically, we estimated the amount of produced  $^{11}\text{C}$  isotopes per penetration depth. Results are shown in figure 11 in comparison with the Monte Carlo predictions. Again, no normalization or scaling factor was applied.

Additionally, the two filter functions and equation (27) were used to calculate the  $^{11}\text{C}$  depth production for a more realistic SOBP (160 mm water-equivalent range, 100 mm water-equivalent modulation,  $80 \times 80 \text{ mm}^2$  aperture,  $\approx 6\mu \text{ Gy}$  maximum dose) irradiation of an inhomogeneous target consisting of 80 mm PMMA, 30 mm lung equivalent ( $w_{\text{C}} = 59.38\%$ ,  $w_{\text{O}} = 18.14\%$ ,  $\rho = 0.3 \text{ g cm}^{-3}$ ,  $\rho_{\text{el}}/\rho_{\text{el,PMMA}} = 0.2554$ ), 30 mm water, 30 mm bone equivalent ( $w_{\text{C}} = 31.41\%$ ,  $w_{\text{O}} = 36.50\%$ ,  $\rho = 1.819 \text{ g cm}^{-3}$ ,  $\rho_{\text{el}}/\rho_{\text{el,PMMA}} = 1.4798$ ). This configuration was chosen to stop the maximum beam energies in the bone-equivalent

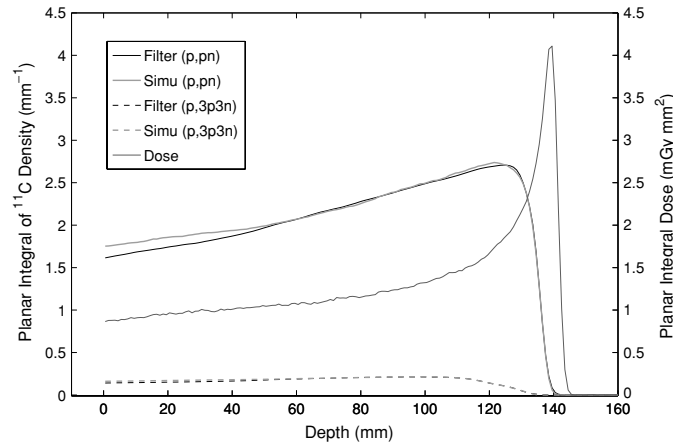


**Figure 10.**  $^{11}\text{C}$  isotope depth profiles (black) obtained by applying two distinct filter functions corresponding to the  $^{12}\text{C}(\text{p}, \text{pn})^{11}\text{C}$  (solid) and  $^{16}\text{O}(\text{p}, 3\text{p}3\text{n})^{11}\text{C}$  (dashed) reaction channels to the same dose distribution (dark grey) for a 152.1 MeV proton irradiation of PMMA ( $10^4$  primaries). The Monte Carlo predictions (light grey) used for the calculation of the filters according to the method described in section 2.3 are also shown.

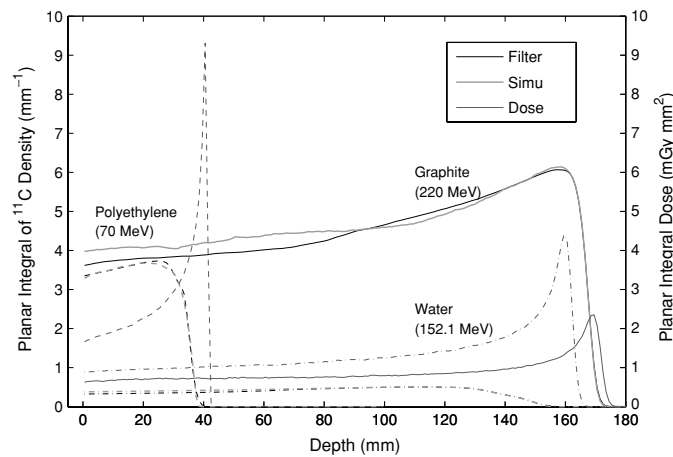


**Figure 11.**  $^{11}\text{C}$  isotope depth profiles (black) obtained from equation (27) using the two filter functions  $f_{\text{C},\text{p,pn}}$  and  $f_{\text{O},\text{p},3\text{p}3\text{n}}$  calculated in PMMA and applied to the Monte Carlo simulated dose distributions (dark grey) for  $10^4$  protons stopped in polyethylene (dashed), water (dash-dotted) and graphite (solid) at 70, 152.1 and 220 MeV initial energies, respectively. The corresponding isotope depth profiles predicted by Monte Carlo are shown in light grey.

insert. Due to the negligible ( $<2\%$ ) amount of nitrogen in the considered equivalent materials as well as the low integral cross section for the  $^{14}\text{N}(\text{p}, 2\text{p}2\text{n})^{11}\text{C}$  reaction, this additional  $^{11}\text{C}$  production channel was neglected. The filtered distribution and the positron emitter prediction obtained from Monte Carlo were finally convolved with a psf of 7 mm FWHM to mimic a realistic response of a PET imaging system. Results are compared in figure 12 for two different lateral integration regions around the central beam axis.

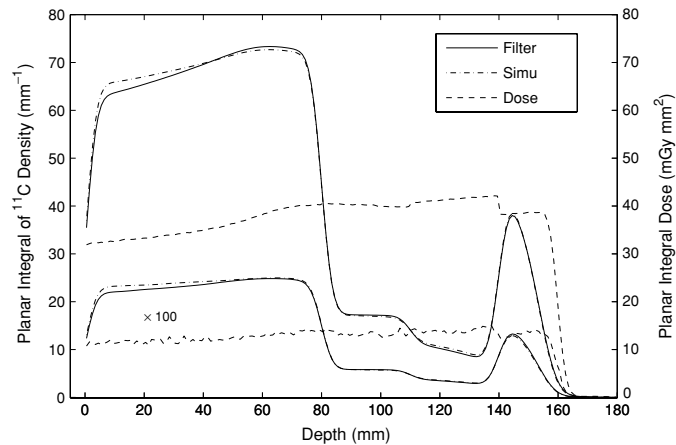


**Figure 12.** SOBP irradiation of an inhomogeneous phantom consisting of 80 mm PMMA, 30 mm lung equivalent, 30 mm water, 30 mm bone equivalent. The  $^{11}\text{C}$  activity profiles (solid) were obtained using equation (27) and the filter functions  $f_{C_{p,pn}}$  and  $f_{O_{p,3p3n}}$  calculated in PMMA and applied to the predicted dose distributions (dashed). They are compared with the  $^{11}\text{C}$  Monte Carlo predictions (dash-dotted). Upper curves refer to data laterally integrated over the whole field. Lower (amplified by a factor of 100) were obtained from a smaller integration region  $\pm 2.5$  mm around the central axis.

## 5. Discussion

It has been shown that a proper filtering of the planned dose distribution can be used to determine the  $\beta^+$ -activation of arbitrary targets along the direction of beam penetration, which is of relevance for range monitoring. The approach has been applied to PET data measured after proton irradiation of a homogeneous phantom, and validated against Monte Carlo calculations in inhomogeneous targets. In all presented results, excellent agreement in position in depth (better than 1 mm) could be achieved between filter-calculated, measured and Monte Carlo simulated activity profiles. In terms of absolute intensity, the agreement was within 1.5% between filtered and simulated profiles and within 10% between filtered and measured data in the distal region of interest. It should be noted that the comparison to the measured data was done for a high dose exposure and long acquisition time, to address the accuracy of the presented calculation method against ideal, high statistics data. A more detailed analysis of the sensitivity of PET measurements to the applied dose and imaging time in view of realistic clinical applications will be addressed in a separate paper.

The filtering model is limited to one spatial dimension along the direction of beam penetration, which is, of course, most relevant for range monitoring. For multifield irradiation, the filtering should be separately applied to the dose distribution of each individual portal, keeping into account the different time of delivery and of delay to the start of imaging. The results should be finally summed up to produce the integral activity distribution to be compared to the PET scan. Clearly, the latter provides the most useful range information in the case of non-opposing fields. By definition, opposing fields are less critical with respect to range uncertainties. For very small fields, the sensitivity of the method to the lateral field extension due to scattering has been removed by entire lateral integration of the distributions. For broad beams, it has been demonstrated that a unique filter function can be used, almost independently of the extension of the lateral integration region. In cases of high curvature of the distal surface of the dose distribution, or for very small stereotactic fields, an extension of the model to two or

three dimensions will be necessary. In other realistic situations, the present one-dimensional model should be applicable.

The proposed method requires a limited number of reaction-dependent filter functions to be calculated in reference materials. This can be done analytically on the basis of the introduced ' $\tilde{Q}$ ' formalism. Unlike full-blown Monte Carlo simulations, the knowledge of tissue parameters (elemental composition, mass and electron density) is required only in the distal region of interest. The local applicability of equation (24) avoids cumulative errors. It makes the method insensitive to conversion errors in the proximal part of the beam penetration, e.g., due to CT artefacts in patient studies. It should also be noted that the one-dimensional stretching of equation (25) is conceptually independent from the real beam interaction. Effects due to finite beam size and lateral heterogeneities in the beam path are already included in the original planned dose distribution and are therefore inherently taken into account.

The accuracy and precision of the method depends primarily on the activation and Bragg-peak pairs,  $p_i(z, R)$  and  $b(z, R)$ , used for the determination of the filter functions  $f_i(z)$  according to the method described in section 2.3. The selection of a specific range,  $R$ , is arbitrary, as has been shown. In our implementation, the lateral field extension has no relevance, due to the lateral integration discussed above. Conversely, the distal depth dependence of  $p_i(z, R)$  and  $b(z, R)$  has a dramatic impact. In particular,  $p_i(z, R)$  critically depends on the cross section values for the given activation reaction channel,  $i$ . Nevertheless, both quantities can be accurately validated through experimental measurements in the selected reference materials.

The proposed approach offers an alternative to Monte Carlo for PET verification of proton therapy. It is simpler and faster, and it intrinsically reflects the accuracy of the treatment planning algorithms. However, it cannot model counting statistics effects for a given prescribed dose distribution. Nevertheless, the calculated amounts can be used as mean values of Poisson sampling similarly to the approach suggested in Inaniwa *et al* (2005). Furthermore, it does not include the explicit description of the imaging formation process (positron and photon propagation). However, the application of a system- (and possibly also material- and position-) dependent point spread function is a useful approximation, as has been shown. The issue is less critical for off-line imaging due to the better imaging performances of full ring tomographs compared to limited-angle in-beam detectors. Furthermore, the off-line approach naturally restricts the imaging to a reduced number of long-lived isotopes which have lower  $\beta^+$ -endpoint energy (i.e., shorter positron range) of 1–3 MeV in comparison to values up to  $\approx 17$  MeV for possible millisecond short-lived reaction products detectable in on-line imaging. Like other state-of-the-art calculation tools for prediction of irradiation induced  $\beta^+$ -activation, no biological effects due to perfusion and washout processes are taken into account. These could be added as probability weighting factors of the produced activity on the basis of available functional information.

The approach is believed to be particularly useful for proton beam irradiation, due the limitation of the  $\beta^+$ -activation to *target fragmentation* as well as the absence of energy- and material-dependent mixed radiation fields originating from *projectile fragmentation* of heavier ion beams. We estimated that in proton therapy the contribution to  $\beta^+$ -activation from secondary particles other than protons is negligible ( $\leq 1$ –3%) even when using passive delivery systems, which decrease the purity of the primary beam (Paganetti *et al* 2004). Similarly, the dose contribution from particles other than primary and secondary protons has been reported to be below  $\approx 0.2\%$  (Paganetti 2002). Hence, both the activity and dose distributions directly reflect the energy spectrum of the proton beam. This guarantees the applicability of a unique filter function to a wide range of beam energies and materials for a given reaction channel.

The method seems to be very practicable for off-line imaging at facilities with continuous delivery using passive beam shaping systems. The off-line strategy restricts the amount of reaction-dependent filter functions to be calculated. In the case of non-negligible time delay between irradiation and imaging (say,  $\Delta t \geq 10$  min), it basically reduces to reaction channels leading to the production of long-lived isotopes. In patient studies these are mainly  $^{11}\text{C}$  and possibly also  $^{13}\text{N}$  ( $T_{1/2} = 9.97$  min) and  $^{38}\text{K}$  ( $T_{1/2} = 7.63$  min), depending on the elemental composition of the activated tissues. Passive beam shaping systems do not pose the complication of dynamic formation of the activity for each individually delivered pencil beam building up the total dose distribution, such as for some active beam scanning systems.

## 6. Conclusion

A novel approach for one-dimensional, quantitative estimation of proton induced activity has been proposed and validated against phantom experiments and Monte Carlo studies. It basically requires a small number of reaction-dependent filter functions calculated in reference materials and applied to the planned dose distributions. Tools for the analytical determination of the filter functions have been provided using a mathematical framework based on Gaussian–powerlaw convolutions.

With the proposed one-dimensional filter model, the crucial problem of range verification can be reasonably tackled. In regions of high curvature of the distal surface of the dose distribution or for very small fields, a two- or three-dimensional approach may be required, which is currently under investigation. Finally, an inversion of the filter functions would allow direct dose quantification from the measured PET distributions. However, this approach requires PET data of excellent signal-to-noise ratio and negligible influence of biological processes. Both requirements are somewhat difficult to fulfil with off-line imaging strategies. Further research on this issue is necessary.

## Acknowledgments

The authors wish to thank E Cascio, J Flanz and H Paganetti from the Proton Therapy Center at Massachusetts General Hospital for experimental support in the presented phantom irradiation. We acknowledge N Alpert and A Bonab from the Department of Radiology of Massachusetts General Hospital and K Lohmann from CPS Innovation (Knoxville, TN) for making the PET/CT scanner available and performing the acquisition and reconstruction of the presented imaged activity. Furthermore, we are grateful to H Paganetti for providing the phase space of the presented SOBP irradiation. This work was supported by NCI Grant 5 P01 CA21239-25 for Proton Radiation Therapy Research.

## Appendix

The convolution of two  $\tilde{Q}_v$  functions is

$$\tilde{Q}_{v_1}(x) * \tilde{Q}_{v_2}(x) = G(x) * P_{v_1}(x) * G(x) * P_{v_2}(x) \quad (\text{A.1})$$

$$= G(x) * G(x) * P_{v_1}(x) * P_{v_2}(x). \quad (\text{A.2})$$

From Gradshteyn and Ryzhik (1980, p 285), we know that

$$P_{v_1}(x) * P_{v_2}(x) = P_{v_1+v_2}(x). \quad (\text{A.3})$$

The convolution of two Gaussians yields

$$G(x) * G(x) = \frac{1}{\sqrt{2}} G\left(\frac{x}{\sqrt{2}}\right). \quad (\text{A.4})$$

Hence, the result is

$$\tilde{Q}_{\nu_1}(x) * \tilde{Q}_{\nu_2}(x) = \sqrt{2}^{\nu_1+\nu_2-2} G\left(\frac{x}{\sqrt{2}}\right) * P_{\nu_1+\nu_2}\left(\frac{x}{\sqrt{2}}\right) \quad (\text{A.5})$$

$$= \sqrt{2}^{\nu_1+\nu_2-1} \tilde{Q}_{\nu_1+\nu_2}\left(\frac{x}{\sqrt{2}}\right). \quad (\text{A.6})$$

If we now consider scaled versions of  $\tilde{Q}_\nu$ , we obtain

$$\tilde{Q}_{\nu_1}\left(\frac{x}{\sigma_1}\right) * \tilde{Q}_{\nu_2}\left(\frac{x}{\sigma_2}\right) \quad (\text{A.7})$$

$$= \frac{1}{\sigma_1 \sigma_2} G\left(\frac{x}{\sigma_1}\right) * P_{\nu_1}\left(\frac{x}{\sigma_1}\right) * G\left(\frac{x}{\sigma_2}\right) * P_{\nu_2}\left(\frac{x}{\sigma_2}\right) \quad (\text{A.8})$$

$$= \frac{1}{\sigma_1 \sigma_2} G\left(\frac{x}{\sigma_1}\right) * G\left(\frac{x}{\sigma_2}\right) * P_{\nu_1}\left(\frac{x}{\sigma_1}\right) * P_{\nu_2}\left(\frac{x}{\sigma_2}\right) \quad (\text{A.9})$$

$$= \frac{1}{\sqrt{\sigma_1^2 + \sigma_2^2}} G\left(\frac{x}{\sqrt{\sigma_1^2 + \sigma_2^2}}\right) * P_{\nu_1}\left(\frac{x}{\sigma_1}\right) * P_{\nu_2}\left(\frac{x}{\sigma_2}\right). \quad (\text{A.10})$$

The convolution of the last two terms on the right-hand side yields

$$P_{\nu_1}\left(\frac{x}{\sigma_1}\right) * P_{\nu_2}\left(\frac{x}{\sigma_2}\right) = \frac{1}{\sigma_1^{\nu_1-1} \sigma_2^{\nu_2-1}} P_{\nu_1}(x) * P_{\nu_2}(x) \quad (\text{A.11})$$

$$= \frac{1}{\sigma_1^{\nu_1-1} \sigma_2^{\nu_2-1}} P_{\nu_1+\nu_2}(x) \quad (\text{A.12})$$

$$= \frac{\sqrt{\sigma_1^2 + \sigma_2^2}^{\nu_1+\nu_2-1}}{\sigma_1^{\nu_1-1} \sigma_2^{\nu_2-1}} P_{\nu_1+\nu_2}\left(\frac{x}{\sqrt{\sigma_1^2 + \sigma_2^2}}\right). \quad (\text{A.13})$$

Consequently,

$$\tilde{Q}_{\nu_1}\left(\frac{x}{\sigma_1}\right) * \tilde{Q}_{\nu_2}\left(\frac{x}{\sigma_2}\right) \quad (\text{A.14})$$

$$= \frac{\sqrt{\sigma_1^2 + \sigma_2^2}^{\nu_1+\nu_2-2}}{\sigma_1^{\nu_1-1} \sigma_2^{\nu_2-1}} G\left(\frac{x}{\sqrt{\sigma_1^2 + \sigma_2^2}}\right) * P_{\nu_1+\nu_2}\left(\frac{x}{\sqrt{\sigma_1^2 + \sigma_2^2}}\right) \quad (\text{A.15})$$

$$= \frac{\sqrt{\sigma_1^2 + \sigma_2^2}^{\nu_1+\nu_2-1}}{\sigma_1^{\nu_1-1} \sigma_2^{\nu_2-1}} \tilde{Q}_{\nu_1+\nu_2}\left(\frac{x}{\sqrt{\sigma_1^2 + \sigma_2^2}}\right). \quad (\text{A.16})$$

Due to the shift invariance of the convolution integral (Bracewell 1986, p 108), we finally obtain

$$\tilde{Q}_{v_1} \left( \frac{x - a_1}{\sigma_1} \right) * \tilde{Q}_{v_2} \left( \frac{x - a_2}{\sigma_2} \right) = \frac{\sqrt{\sigma_1^2 + \sigma_2^2}^{v_1+v_2-1}}{\sigma_1^{v_1-1} \sigma_2^{v_2-1}} \tilde{Q}_{v_1+v_2} \left( \frac{x - a_1 - a_2}{\sqrt{\sigma_1^2 + \sigma_2^2}} \right). \quad (\text{A.17})$$

## References

- Agostinelli S *et al* 2003 GEANT4—a simulation toolkit *Nucl. Instrum. Methods A* **506** 250–303
- Albouy G, Cohen J P, Gusakov M, Poffe N, Sergolle H and Valentin L 1962 Spallation de l'oxygene par des protons de 20 a 150 MeV *Phys. Lett.* **2** 306–7
- Bennett G W, Archambeau J O, Archambeau B E, Meltzer J I and Wingate C L 1978 Visualization and transport of positron emission from proton activation *in vivo Science* **200** 1151–3
- Bortfeld T 1997 An analytical approximation of the Bragg curve for therapeutic proton beams *Med. Phys.* **24** 2024–33
- Bracewell R N 1986 *The Fourier Transform and Its Applications* 2nd edn (New York: McGraw-Hill)
- Enghardt W, Crespo P, Fiedler F, Hinz R, Parodi K, Pawelke J and Pönisch F 2004a Charged hadron tumour therapy monitoring by means of PET *Nucl. Instrum. Methods A* **525** 284–8
- Enghardt W, Debus J, Haberer T, Hasch B G, Hinz R, Jäkel O, Krämer M, Lauckner K, Pawelke J and Pönisch F 1999 Positron emission tomography for quality assurance of cancer therapy with light ion beams *Nucl. Phys. A* **654** 1047c–1050c
- Enghardt W, Parodi K, Crespo P, Fiedler F, Pawelke J and Pönisch F 2004b Dose quantification from in-beam positron emission tomography *Radiother. Oncol.* **73** S96–8
- Fassò A, Ferrari A, Ranft J and Sala P R 2001a FLUKA: status and prospective for hadronic applications *Proc. Monte Carlo 2000 Conference (Lisbon)* ed A Kling, F Barao, M Nakagawa, L Tavora and P Vaz (Berlin: Springer) pp 955–60
- Fassò A, Ferrari A and Sala P R 2001b Electron–photon transport in FLUKA: status *Proc. Monte Carlo 2000 Conference (Lisbon)* ed A Kling, F Barao, M Nakagawa, L Tavora and P Vaz (Berlin: Springer) pp 159–64
- Gradshteyn I S and Ryzhik I M 1980 *Table of Integrals, Series and Products* corrected and enlarged edn (San Diego: Academic)
- Hishikawa Y, Kagawa K, Murakami M, Sakai H, Akagi T and Abe M 2002 Usefulness of positron-emission tomographic images after proton therapy *Int. J. Radiat. Oncol. Biol. Phys.* **53** 1388–91
- Hong L, Goitein M, Bucciolini M, Comiskey R, Gottschalk B, Rosenthal S, Serago C and Urie M 1996 A pencil beam algorithm for proton dose calculations *Phys. Med. Biol.* **41** 1305–30
- Inaniwa T, Tomitani T, Kohno T and Kanai T 2005 Quantitative comparison of suitability of various beams for range monitoring with induced  $\beta^+$  activity in hadron therapy *Phys. Med. Biol.* **50** 1131–45
- Litzenberg D W, Roberts D A, Lee M Y, Pham K, Vander Molen A M, Ronningen R and Becchetti F D 1999 On-line monitoring of radiotherapy beams: experimental results with proton beams *Med. Phys.* **26** 992–1006
- Nishio T, Sato T, Kitamura H, Murakami K and Ogino T 2005 Distributions of  $\beta^+$  decayed nuclei generated in the  $\text{CH}_2$  and  $\text{H}_2\text{O}$  targets by target nuclear fragment reaction using therapeutic MONO and SOBP proton beam *Med. Phys.* **32** 1070–82
- Oelfke U, Lam G K Y and Atkins M S 1996 Proton dose monitoring with PET: quantitative studies in lucite *Phys. Med. Biol.* **41** 177–96
- Paans A M J and Schippers J M 1993 Proton therapy in combination with PET as monitor: a feasibility study *IEEE Trans. Nucl. Sci.* **40** 1041–4
- Paganetti H 2002 Nuclear interactions in proton therapy: dose and relative biological effect distributions originating from primary and secondary particles *Phys. Med. Biol.* **47** 747–64
- Paganetti H, Jiang H, Lee S-Y and Kooy H 2004 Accurate Monte Carlo simulations for nozzle design, commissioning and quality assurance for a proton radiation therapy facility *Med. Phys.* **31** 2107–18
- Parodi K, Enghardt W and Haberer T 2002 In-beam PET measurements of  $\beta^+$ -radioactivity induced by proton beams *Phys. Med. Biol.* **47** 21–36
- Parodi K, Pönisch F and Enghardt W 2005 Experimental study on the feasibility of in-beam PET for accurate monitoring of proton therapy *IEEE Trans. Nucl. Sci.* **52** 778–86
- Pönisch F, Parodi K, Hasch B G and Enghardt W 2004 The description of positron emitter production and PET imaging during carbon ion therapy *Phys. Med. Biol.* **49** 5217–32
- Vynckier S, Derreumaux S, Richard F, Bol A, Michel C and Wambersie A 1993 Is it possible to verify directly a proton-treatment plan using positron emission tomography? *Radiother. Oncol.* **26** 275–7